Journal of Power Sources 359 (2017) 322–331

Contents lists available at ScienceDirect

Journal of Power Sources

journal homepage: www.elsevier.com/locate/jpowsour

Mass transport enhancement in redox flow batteries with corrugated fluidic networks

Kleber Marques Lisboa [a, b], Julian Marschewski [a, c], Neil Ebejer [c], Patrick Ruch [c], Renato Machado Cotta [b], Bruno Michel [c], Dimos Poulikakos [a, *]

[a] Laboratory of Thermodynamics in Emerging Technologies, Department of Mechanical and Process Engineering, ETH Zürich, 8092 Zürich, Switzerland
[b] Laboratory of Nano- and Microfluidics and Microsystems, LabMEMS, Mechanical Engineering Dept. (PEM) & Nanoengineering Dept. (PENT) – POLI&COPPE, UFRJ, Universidade Federal do Rio de Janeiro, Cidade Universitária, Cx. Postal 68503, Rio de Janeiro, RJ, CEP 21945-970, Brazil
[c] IBM Research Zurich, Säumerstrasse 4, 8803 Rüschlikon, Zürich, Switzerland

HIGHLIGHTS

- Experimental study of mass transport in small-scale redox flow batteries.
- Corrugated walls greatly enhance mass transport of electrolytes in the electrode.
- Limiting current scaling with $Re^{0.74}$.
- Net power density doubled in comparison to the conventional flow-by configuration.

GRAPHICAL ABSTRACT

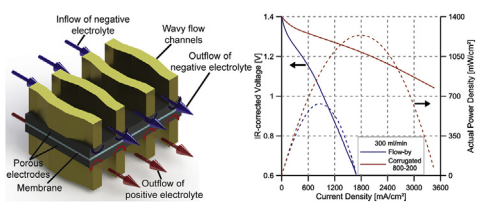

ARTICLE INFO

Article history:
Received 27 March 2017
Received in revised form
12 May 2017
Accepted 13 May 2017
Available online 30 May 2017

Keywords:
Redox flow battery
Corrugated wall fluidics
Mass transport enhancement

ABSTRACT

We propose a facile, novel concept of mass transfer enhancement in flow batteries based on electrolyte guidance in rationally designed corrugated channel systems. The proposed fluidic networks employ periodic throttling of the flow to optimally deflect the electrolytes into the porous electrode, targeting enhancement of the electrolyte-electrode interaction. Theoretical analysis is conducted with channels in the form of trapezoidal waves, confirming and detailing the mass transport enhancement mechanism. In dilute concentration experiments with an alkaline quinone redox chemistry, a scaling of the limiting current with $Re^{0.74}$ is identified, which compares favourably against the $Re^{0.33}$ scaling typical of diffusion-limited laminar processes. Experimental IR-corrected polarization curves are presented for high concentration conditions, and a significant performance improvement is observed with the narrowing of the nozzles. The adverse effects of periodic throttling on the pumping power are compared with the benefits in terms of power density, and an improvement of up to 102% in net power density is obtained in comparison with the flow-by case employing straight parallel channels. The proposed novel concept of corrugated fluidic networks comes with facile fabrication and contributes to the improvement of the transport characteristics and overall performance of redox flow battery systems.

© 2017 Elsevier B.V. All rights reserved.

1. Introduction

With rising awareness and scientific evidence that human activity plays a major role in global warming, the demand for replacement of fossil-fuel-based energy sources in favour of renewable sources in both mobile and stationary applications has greatly increased. However, most of the renewable energy sources available suffer from intermittent energy output during operation, as is the case of solar and wind power, for example, rendering them

* Corresponding author.
E-mail address: dpoulikakos@ethz.ch (D. Poulikakos).

http://dx.doi.org/10.1016/j.jpowsour.2017.05.038
0378-7753/© 2017 Elsevier B.V. All rights reserved.

unsuitable for covering most of the energy demand by themselves. To overcome this challenge, development of efficient energy storage technologies is considered to be crucial [1,2]. One attractive option is the redox flow battery (RFB), mainly due to its characteristic decoupling between the amount of energy stored (related to the electrolyte tank volume) and the rated power (related, considering all other conditions the same, to the size of the cell) [3]. This technology was pioneered by NASA-Lewis Research Center with the Fe/Cr concept [4,5], but the research started gaining commercial momentum after the invention of the all-vanadium flow battery [6]. A typical RFB usually consists of stacks of several cells responsible for converting electrical energy into chemical energy and vice versa.

In addition to large-scale applications, miniaturization of RFBs could open up new applications, helping the technology to overcome the cost barrier that has prevented it from gaining widespread usage [7]. Among the applications that could benefit from distributed and miniaturized RFBs, the electronics industry is highlighted. The integration of RFBs with electronic components could allow for a dual function application in which the redox flow cell is responsible for both power delivery and cooling. In data centres, for example, there is a prospective enhancement in energy efficiency by combining heat removal [8] and power delivery in a single module. This system would work simultaneously as a combined RFB and heat exchanger capable of complementing or even completely substituting conventional technologies. The direct integration of power-delivering RFBs with electronic components on the same substrate allows to reduce the number of power connections, voltage transformation steps, and total wiring length [9]. These characteristics could lead to more space for logical connections and reduced cost of the energy supply to data centres [10–12].

The aforementioned integration requires an effort to reduce the size of RFBs to match the footprint of the electronic devices (i.e. of the order of cm^2 for a microprocessor) and also to increase the power density to cope with the high demand for electrical input. The downscaling also can potentially decrease the cost of the cell due to a smaller area of the expensive membrane and overall cell size [13,14]. This need imposes a different emphasis in comparison with mainstream research in RFBs, which targets predominantly energy and voltage efficiencies rather than power density. This assertion can be stressed noticing that most power densities previously reported in the literature for RFBs are substantially less than 1 W cm^{-2} [15–18]. However, the benefits of high power density RFBs are not restricted to the particular application in electronic devices, and some groups have pursued higher power densities in their works as a means to achieve cost reduction [19–21].

With maximum power density as the primary objective and analysing the polarization curve performance of such cells, there are three main contributions to the deviation from ideal flat polarization curves: kinetic losses, ohmic losses, and mass transport deficiency. Additionally, the pressure drop becomes a crucial factor in the overall performance of cells with small channels, since it is directly proportional to the pumping losses. From the aforementioned loss mechanisms, the mass transport deficiency is the main focus of this work. A major strategy for enhancing mass transport in an RFB is a rational design of the fluidic networks directing the flow of electrolytes. Amongst the designs of fluidic networks reported in literature, three of them are highlighted here. The first one is the basic flow-through, in which the entire volume of electrolyte flow is forced to enter a porous electrode placed within a channel. This design allows for the lowest mass-transport-related losses, but has the serious disadvantage of being restricted to lower flow rates due to high pressure drops imposed by the porous medium [22,23]. The other extreme in this trade-off between mass transport and pressure drop is the flow-by concept. Usually applied either with parallel or serpentine channels, it offers, in the parallel case, the poorest mass transport performance because the flow-by concept relies mostly on diffusion. Its most beneficial feature is having very small pressure drops in comparison with the flow-through approach [15,23–25]. An intermediate approach between the two aforementioned is the interdigitated fluidic network [23,25,26]. It aims at a better balance between the flow-through and the flow-by configurations by positioning parallel channels alternately with one of the ends of the channel closed. This way the fluid still flows mostly inside open channels, while being forced to eventually cross through the porous electrode positioned on top of the fluidic network to the adjacent channel. This approach rendered very good results, with a power density of 1.3 W cm^{-2} being reported for an all-vanadium redox flow battery [19]. More recently, improvements of the interdigitated concept were proposed by adding tapering and multiple-passing [27]. The tapering was introduced to homogenize the flow and, hence, to reduce the mass transport resistance due to depletion of electrolytes in certain areas of the carbon paper. The multiple-pass strategy is aimed at raising the conversion of the electrolyte beyond the single-pass limit and effectively increased the superficial velocity within the porous domain of the electrode. Promising results were achieved with a maximum produced power of 1.4 W cm^{-2} reported for an alkaline quinone flow battery chemistry [27].

The present work proposes a novel perspective on fluidic networks with the introduction of corrugated channels alternating periodically between a constriction and an expansion in contrast to commonly used straight channels. Corrugated fluidic networks have already been reported [28,29]. However, the previously studied wavy patterns were perpendicular to the membrane plane, in contrast to the parallel configuration employed in this work. This design is intended to partially deflect the electrolyte flow into porous electrode. The basic wave chosen to construct each wall is trapezoidal. Our corrugated channel concept combines advantages of previously reported fluidic networks, as all the previously mentioned geometries can be considered as extreme cases driving none or the entire flow through the porous electrode. With the choking of the flow at the narrowest sections of the present corrugated channels, only part of the electrolyte flow is driven through the porous electrodes, whilst the remaining liquid stays in the channel. This offers significant flexibility in optimizing the design between maximizing mass transfer and minimizing pressure drop.

To investigate the postulated mass transport enhancement mechanism with the introduction of the corrugated channel concept, first, a computational fluid dynamics (CFD) analysis was conducted. Based on computational findings, 3D-printed fluidic networks with the novel geometry were subsequently fabricated with different degrees of narrowing of the flow path. Currently available rapid prototyping techniques were chosen to allow for inexpensive and versatile manufacturing of the fluidic networks [30]. In total, four different fluidic networks were compared. The flow-by configuration with straight, parallel channels was used as a benchmark, since its characteristics are well known. The other three are detailed in the sections to follow. Initially, low concentration measurements with the alkaline quinone redox chemistry [18] were carried out due to the dominance of mass-transport-related overpotentials at low concentrations. This fact allows for a direct assessment of the mass transport characteristics with the help of the limiting current density. Subsequently, high concentration measurements, close to saturation of the catholyte, were performed and the polarization curves were measured and analysed for each design iteration of the fluidic networks. The effect of the fluidic network on the overall performance of the RFB,

considering minimizing concentration polarization as the main adjustable parameter was thoroughly investigated. The scaling of current density at a certain potential with a characteristic Reynolds number is also presented. Finally, the balance between produced power and pumping power as a function of volume flow rate is discussed. Each design supports a distinct optimum range of operation, and overall all designs exhibited a significant performance improvement in comparison to the flow-by fluidic networks.

2. Experimental

2.1. Flow cell

Following the design indicated in Fig. 1b, fluidic networks were manufactured by 3D-LABS GmbH (St. Georgen, Germany) using a 3D Systems machine (ProJet HD 3000Plus) with VisiJet EX200 Plastic. The corrugated wall channels were arranged in a space-efficient interlocked manner. The different designs were labelled according to the dimensions indicated in the detailed view shown in Fig. 1b, and are summarized in Table 1. Henceforth, these labels shall be used to refer to the different sizes. The horizontal segment of the trapezoid, indicated as L in Fig. 1b, has a length of 500 μm for all the cases studied. To avoid any preferable path for the fluid that would lead to low flow rates in some channels, the design was carried out with 5 1/2 periods of the basic trapezoidal wave pattern. This design decision aims at putting the same number of features (nozzles or expansions) in the flow path inside each channel, ensuring all parallel channels present the same pressure drop to the flow in order to ensure an equal distribution of the flow. The dimensions of the area occupied by the corrugated wall structures were 1 cm × 1 cm, the channel walls thickness was 250 μm, and the channel height was 600 μm. The aforementioned area of 1 cm^2 shall be used as reference to report the electrochemical measurements data. The commercially available DuPont Nafion 115, that was pretreated as described in Ref. [18], was used in the low concentration experiments, whilst DuPont Nafion 211, also treated and stored in the same manner [18], was used for the high concentration experiments. Two porous electrodes (Spectracarb 2050A-1050 by Engineered Fibers Technology, LLC, USA, pretreated by baking at 400 °C in air for 30 h) were cut with the dimensions of 1.8 cm × 1 cm and placed on each side of the membrane. Fig. 1a illustrates a section of the mounting of the most important functional parts of the cell along with an indication of the direction of the flow of both the catholyte and anolyte. In the dilute concentration experiments, current collection and sealing was realized by two resin-filled graphite plates (FC-GR347B by Graphtek LLC, USA), that were machined to fit the 3D-printed parts. For the high concentration measurements, current collection was achieved by four 600 μm thick expanded graphite current collectors (Sigracell TF6, kindly supplied by SGL CARBON GmbH, Germany), two on each side, which were cut to fit the fluidic networks. Spacers made of glass fibre-reinforced PTFE (Maagtechnic AG, Switzerland) were placed around the electrodes in order to achieve an electrode compression of around 25% and also for sealing purposes. Custom designed PVC manifolds were placed on both ends and the whole system was held together with the help of bolted aluminium end plates. To ensure reproducible contact resistance and sealing, four M8 bolts positioned near the four vertices of the aluminium end plates were tightened until a torque of 5 N m was reached.

Table 1
Definition of labels for the different designs tested. L = 500 μm for all designs.

Label	d (μm)	w (μm)
500–500 (flow-by)	500	500
600–400	600	400
700–300	700	300
800–200	800	200

2.2. Flow loop and pressure measurements

PFA tubing in combination with stainless steel fittings (Swagelok, USA and Serto AG, Switzerland) were used in the assembly of the flow loop. The flow of both positive and negative electrolytes was achieved with magnetically coupled gear pumps (Fluid-o-Tech s.r.l., Italy) and the volume flow rate was measured with two Coriolis flow meters (Cubemass DCI by Endress + Hauser AG, Switzerland and Optimass 3000 by Krohne GmbH, Germany). To measure the pressure drop, a differential pressure gauge (PD23 by Omega Engineering Inc., USA) was positioned on a T-fitting at the in- and outlet of one half-cell of the electrochemical system. A schematic drawing of the flow loop is given in Supplementary Fig. SI1. Electronic terminal blocks (Beckhoff Automation,

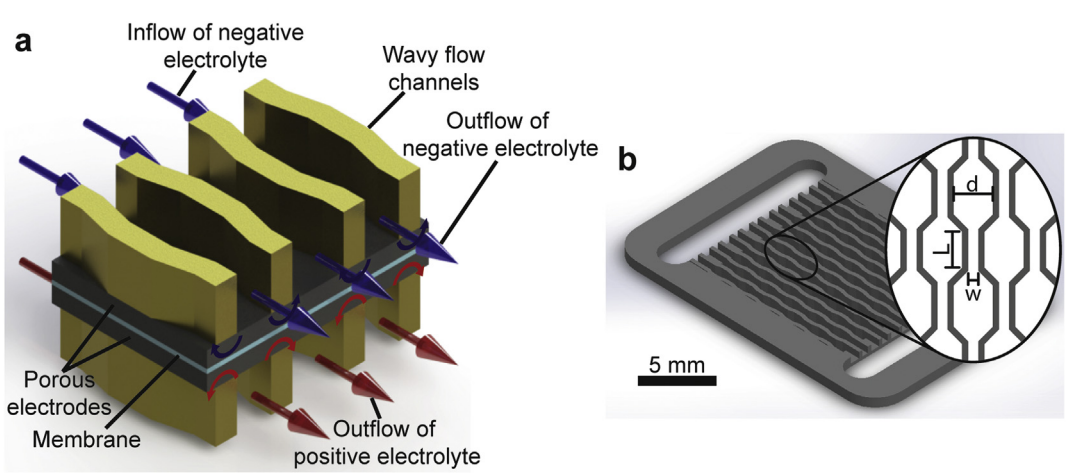

Fig. 1. Corrugated wall fluidic network concept. (a) Illustration of a section of the most important functional parts of the cell. The flow direction and the postulated flow path within the porous electrode are also indicated (not to scale). (b) Isometric and detailed view of the design of the 3D-printed fluidic networks. The pattern of each channel wall is of a trapezoidal wave. Dimensions are indicated in the detailed view, d is the width of the channel at the widest section, w the width of the channel at the narrowest section, and L is the length of the horizontal segment of the trapezoid.

Germany) in combination with a LabVIEW interface were used for parts of the data acquisition.

2.3. Electrochemical measurements

A recently reported alkaline-based redox system [18] was chosen for these experiments for its non-toxic, inexpensive and rather fast kinetics in comparison with most of the previously reported chemistries [31,32]. 2,6-dihydroxyanthraquinone (2,6-DHAQ) was purchased from AK Scientific Inc., USA (95% purity) and potassium hexacyanoferrate(II) trihydrate (potassium ferrocyanide) was acquired from Sigma-Aldrich (≥98.5% purity). Both were dissolved as received in KOH solutions prepared by dilution from 44% KOH (Technic France, VLSI grade). For the dilute concentration experiments, the catholyte solution was prepared with 5 mM of $K_4Fe(CN)_6$, while the anolyte solution had 2.5 mM of 2,6-DHAQ. The supporting electrolyte was 1 M KOH. The high concentration solutions consisted of 0.4 M $K_4Fe(CN)_6$ prepared with 1 M KOH solution for the catholyte and 0.2 M 2,6-DHAQ prepared with 2 M KOH solution for the anolyte. The reason for the concentration of 2,6-DHAQ being half of the one for $K_4Fe(CN)_6$ in the two experimental campaigns is to respect the stoichiometric balance of the overall reaction. The use of a supporting electrolyte with higher concentration in the 2,6-DHAQ solution is intended to better balance the concentration of potassium ions on the two sides of the flow battery. The justification for this decision is the introduction of 4 M of potassium ions for each M of $K_4Fe(CN)_6$ [18]. All polarization curves, electrochemical impedance spectroscopy (EIS), and also charging of the solutions were performed using a BioLogic (France) SP-300 potentiostat including a booster kit. Polarization curves were obtained by scanning from open-circuit voltage to 0.005 V at 50 mV s^{-1}.

3. Modelling of the mass transport phenomena

The geometry in Fig. 2 was proposed as a basis for both the fluid flow and mass transport models that are described in the following sections. The geometry consists of parallel channels with walls constructed with 5 1/2 periods of a trapezoidal wave pattern. Only one half cell was evaluated with the electrolyte properties equivalent to the species with the lowest diffusivity, which indicates the most mass-transport-limited side. The negative of the channel walls, needed for CFD purposes, is presented in Fig. 2b. The isometric view of Fig. 2a shows the placement of the electrode on top of the wave pattern equivalent to the configuration in Fig. 1a. The dimensions assumed in the model were the same as those used in the experimental investigation.

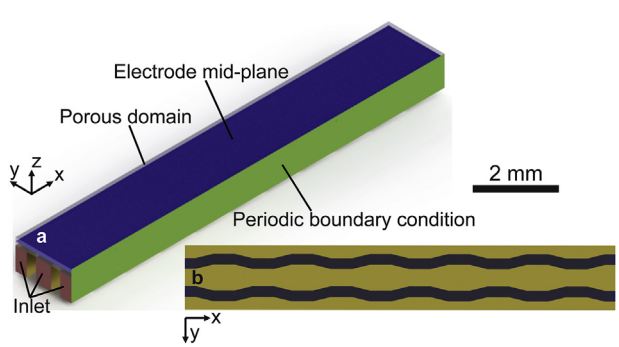

Fig. 2. CFD model of the proposed geometry. (a) Isometric view with indication of the positioning of the porous electrode, the applied boundary conditions, and the mid-plane inside the electrode (in blue). (b) Bottom view detailing the proposed corrugated wall channel geometry. (For interpretation of the references to colour in this figure legend, the reader is referred to the web version of this article.)

3.1. Fluid flow model

For the free fluid flow between the channel walls, standard steady-state, with negligible body forces, incompressible 3D continuity and Navier-Stokes equations were used as detailed below:

$$\nabla \cdot \boldsymbol{u} = 0 \tag{1}$$

$$(\boldsymbol{u} \cdot \nabla)\boldsymbol{u} = -\frac{1}{\rho}\nabla p + \nu \nabla^2 \boldsymbol{u} \tag{2}$$

where $\boldsymbol{u}$ is the velocity vector for the flow of electrolytes within the channels, ρ is the electrolyte density, p is pressure, and ν is the kinematic viscosity.

As for the fluid flow inside the porous electrode, the Darcy-Brinkman model was deemed the most adequate and can be written as [33–36]:

$$\nabla \cdot \boldsymbol{u_p} = 0 \tag{3}$$

$$0 = -\frac{1}{\rho}\nabla p_p + \frac{\nu}{\varepsilon}\nabla^2 \boldsymbol{u_p} - \nu \boldsymbol{K}^{-1}\boldsymbol{u_p} \tag{4}$$

where $\boldsymbol{u_p}$ is the volume averaged velocity vector for the flow of electrolytes within the porous electrode, p_p is the volume averaged pressure within the porous electrode, ε is the porosity, and $\boldsymbol{K}$ is a diagonal permeability matrix that takes into account the different through-plane and in-plane permeability of the porous electrode.

Referring to Fig. 2a, the boundary conditions for fluid flow were a prescribed mass flow rate (consistent with 1/13 of the flow rate for a whole cell) at the inlets, null manometric pressure at the outlet (applied to the opposite faces relative to the inlets in the figure), periodic boundary condition between the two lateral faces, continuity of velocity and stress at the interface between the free flow and electrode with an effective viscosity for the porous side ($\nu_{eff} = \nu/\varepsilon$) [36] and no slip wall boundary condition to the remainder.

3.2. Mass transport model

The governing equations for species conservation for the flow inside the channels can be written as:

$$\boldsymbol{u} \cdot \nabla c = D \nabla^2 c \tag{5}$$

where c is the local concentration of the species and D is the diffusivity of the species.

Within the porous electrode, the model is similar to the one shown in Eq. (5), except for the introduction of the concept of effective diffusivity and the presence of a source term. Such a model is presented below:

$$\boldsymbol{u_p} \cdot \nabla c_p = D_{\text{eff}} \nabla^2 c_p + S \tag{6}$$

where c_p is the volume averaged concentration of the species, D_{eff} is the effective diffusivity and S is the source term. The effective diffusivity can be determined from the diffusivity of the species with the following Bruggeman model [37]:

$$D_{\text{eff}} = \varepsilon^{1.5} D \tag{7}$$

The source term is related to the convective mass transport and the consumption of the reactant at the reaction sites during

discharge. It consists of a semi-empirical relation stating that the reaction rate is proportional to the difference between the bulk concentration of the species and the concentration at the reaction site. To investigate the mass transport in an isolated manner, it was proposed that the limiting current density conditions are applied and the concentration at the reaction site was considered to be zero. In other words, it was assumed that the electrolyte is instantaneously consumed when in contact with the fibre of the electrode. This assumption is appropriate given a large timescale difference between delivery of electrolytes to the reaction sites and the consumption of electrolytes via the electrochemical reactions. Such a timescale difference is typical of mass transport limited regimes. The final expression then stays as follows [38]:

$$S = -ak_m c_p \tag{8}$$

where a is the specific surface area of the porous electrode and k_m is the convective mass transport coefficient. The latter can be determined with the help of the following empirical correlation for fibrous porous media [39]:

$$k_m = 7\frac{D}{d_f}\left(\frac{|\boldsymbol{u_p}|d_f}{\nu}\right)^{0.4} \tag{9}$$

where $|\boldsymbol{u_p}|$ is the magnitude of the velocity vector within the porous electrode and d_f is the fibre diameter.

We refer to Fig. 2a to establish the appropriate boundary conditions for the equations of conservation of species presented so far in this section. At the inlet, a uniform concentration of 0.2 M of an electrolyte involved in a two electron reaction (consistent with the 2,6-DHAQ reaction) was applied, while a no diffusive flux condition was applied to the outlet, that is localized at the exact opposite side relative to the inlets. Periodic boundary conditions were applied between the two lateral faces. For all the other external faces an impermeable wall condition was used. At the interface between the porous media and the free flow domain, both continuity of concentration and flux of electrolyte were imposed.

3.3. Modelling parameters

To complete the modelling process, the set of properties summarized in Table 2 was assumed for the electrolyte solution.

3.4. Meshing and solution procedure

A finite element analysis is conducted with the described model using the commercial software *COMSOL Multiphysics 5.2*. The mesh was based on tetrahedral elements whose sizes were monotonically decreased to obtain numerical convergence of the limiting current. In the faces subjected to no-slip wall condition, an inflated mesh with 5 layers was applied to capture the big gradients of the boundary layer. The solution is divided in two steps. The first is responsible for the fluid flow solution and the second for the mass transport model. For both of them the iterative GMRES solver is used.

Table 2
Properties of the electrolyte and the porous electrode.

Electrolyte properties				
Quantity	**Symbol**	**Value**	**Unit**	**Source**
Density	ρ	1096.7	kg m^{-3}	[27]
Diffusivity of 2,6-DHAQ	D	4.8×10^{-10}	m^2 s^{-1}	[18]
Kinematic viscosity	ν	1.37×10^{-6}	m^2 s^{-1}	[27]
Electrode properties				
Quantity	**Symbol**	**Value**	**Unit**	**Source**
Porosity	ε	0.7	–	Estimated
Fibre diameter	d_f	10	μm	Estimated
Specific surface area	a	73308	m^{-1}	Estimated
In-plane permeability	–	2×10^{-11}	m^2	Estimated
Through plane permeability	–	6×10^{-12}	m^2	Estimated

3.5. Post-processing

A parameter termed volumetric current density is introduced as a local measurement of electrolyte availability and mass transport capability. The expression for this current density, considering the oxidation of 2,6-DHAQ, is given by:

$$i = 2ak_m c_p F \tag{10}$$

where i is the volumetric current density and F is Faraday's constant (96485 C mol^{-1}).

4. Results and discussion

4.1. Simulation results

Fig. 3a–d compare the proposed 600–400, 700–300 and 800–200 (refer to the *d-w* labelling from Table 1 and Fig. 1b) corrugated wall fluidic networks to the flow-by fluidic network with parallel channels. The figures show the mentioned volumetric current density distribution at the mid-plane of the porous electrode (shown in blue in Fig. 2a) for a total volumetric flow rate of 200 ml min^{-1} for a cell with 13 channels. It is evident that the novel geometry is superior in providing higher volumetric current densities. Moreover, the novel fluidic network also mitigates the concentration of current generation near the entrance when comparing the corrugated fluidic networks cases (Fig. 3b–d) with

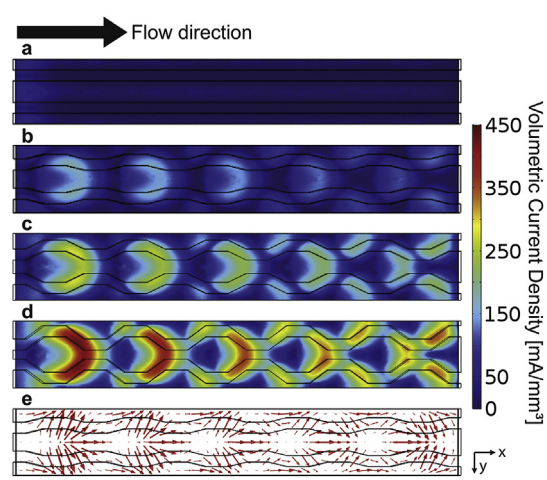

Fig. 3. Fluid flow and mass transport comparison between the novel geometry and the flow-by configuration for a total volumetric flow rate of 200 ml min^{-1} in a cell with 13 channels. (a) Volumetric current density distribution in the mid-plane within the electrode (shown in blue in Fig. 2a) for the flow-by configuration with straight parallel channels case. (b) Volumetric current density distribution in the mid-plane within the electrode (shown in blue in Fig. 2a) for the 600–400 corrugated wall fluidic network. (c) Volumetric current density distribution in the mid-plane within the electrode (shown in blue in Fig. 2a) for the 700–300 corrugated wall fluidic network. (d) Volumetric current density distribution in the mid-plane within the electrode (shown in blue in Fig. 2a) for the 800–200 corrugated wall fluidic network. (e) Velocity arrows in the mid-plane within the electrode (shown in blue in Fig. 2a) for the 600–400 corrugated wall fluidic network. (For interpretation of the references to colour in this figure legend, the reader is referred to the web version of this article.)

the flow-by case with straight channels (Fig. 3a). The distribution of the volumetric current density in the corrugated fluidic networks (Fig. 3b–d) seems to concentrate above the walls just before the beginning of the zone with the narrowest channel cross section (i.e. before the nozzle). To better understand this phenomenon, Fig. 3e shows the velocity vectors for the 600–400 fluidic network in the same plane where the volumetric current density is plotted in Fig. 3b. It is observed that the fluid tends to cross the porous electrode zone when confronted with a constriction, whereby this crossing takes place either above the channel walls into an adjacent channel or above the nozzle into the next channel expansion. The appearance of the former path, i.e. above the convergent channel walls leading to the nozzle, is attributed to a lower pressure loss in the adjacent channels undergoing expansion. On the other hand, the latter path, above the nozzle itself, acts as a shortcut to the broader channel section ahead in the same channel and is preferred by the fluid to minimize energy losses. By taking into account these two flow paths, both the electrolyte availability and the superficial velocity within the porous electrode are increased. These two improvements yield a superior mass transport behaviour in comparison to a mostly diffusion-dominated regime in the parallel flow-by case, which translates into higher volumetric current densities. Similar reasoning can be applied to reach the same conclusions for the other two fluidic networks depicted in Fig. 3c and d and Supplementary Figs. SI2a,b. A simple integration of the volumetric current density over the volume of the porous electrode suggests a ~150% improvement in limiting current density when the 600–400 corrugated wall design is employed, in comparison to the flow-by design with straight channels. This increase of limiting current density reaches up to 4× when the 800–200 design is compared to the flow-by case. The enhancement with narrower nozzles is attributed to the increased flow of electrolytes which crosses either the walls or the nozzles, and visualizes the underlying mechanism of mass transport enhancement.

A depletion effect is observed as the fluid flows downstream from the inlet. This phenomenon is attributed to the time and distance required to reach a developed flow regime in which the same pattern repeats itself periodically. However, this observation refers only to a localized depletion of the electrolytes, since the predicted current densities were still much lower (3.6 A cm^{-2} for the 800–200 case) than the total chemical input assuming full conversion (130 A cm^{-2}). This difference in current densities indicates that the larger portion of the fluid stays between the channels walls all the time without undergoing electrochemical reactions.

4.2. Electrochemical characterization at low concentrations

In Fig. 4a the polarization curves obtained at low electrolyte concentrations (5 mM $K_4Fe(CN)_6$ and 2.5 mM 2,6-DHAQ) and a volume flow rate of 200 ml min^{-1} are presented. From the polarization curves, we conclude that the introduction of the proposed corrugated geometry significantly increases the performance in comparison to the benchmark parallel flow-by configuration. In fact, the mass-transport-limited current (referred to here as limiting current) experiences roughly a fivefold increase with the relatively small change from the 500–500 to the 600–400 configuration (following the *d-w* nomenclature according to Table 1 and Fig. 1b). Similar improvements are seen when comparing these two configurations with the 700–300 and 800–200 cases as they show a 9× and 12× increase in the limiting current in comparison with the 500–500 configuration, respectively. These results underscore the efficacy of the proposed geometry. Table 3 summarizes the limiting currents obtained both numerically and experimentally for a volumetric flow rate of 200 ml min^{-1} for all the cases studied. The simulation results are found to be significantly inaccurate, especially for the corrugated fluidic networks with relative errors of up to 61%. Possible shortcomings of the model include neglection of edge effects, uncertainties regarding electrode properties, and deviation from the nominal dimensions due to fabrication imprecision. However, the model is assumed to be qualitatively close to reality.

In addition to the limiting current improvement, Fig. 4a shows a remarkable enhancement in power density with the use of the corrugated channels architecture. The gain in maximum produced power goes from ~4× when comparing the 600–400 design to the benchmark 500–500 design, to up to ~6× for the 800–200 design versus the flow-by case.

Fig. 4b shows the limiting current behaviour with respect to the Reynolds number based on the smallest cross section of the channels in a double-logarithmic graph. Such a limiting current plot provides further insight into the benefits of the proposed channel geometry in comparison to the parallel channel flow-by configuration. The choice for the definition of the Reynolds number is substantiated by the indication of Fig. 3b,e, i.e. the mass transport enhancement mechanism acts mainly at the entrances of the narrower portions of the channels. The velocity used in the definition of the Reynolds number is determined assuming that the volume flow rate is distributed evenly amongst the channels and that only a small fraction is able to enter the electrode. Again, a rather abrupt improvement is observed with only a slight change from the 500–500 to the 600–400 fluidic network, as it was already highlighted in the previous paragraph. In fact, a consistent overall improvement is observed in the limiting current with narrower nozzles. This increased limiting current indicates that the narrowing indeed increases the flow of the electrolyte through the porous electrode, which leads to a higher fluid volume being swept within the electrode. The mass transport enhancement is observed to diminish with each successive narrowing of the nozzle aperture from the flow-by (500–500) towards the 800–200 design, especially when comparing the 700–300 and 800–200 fluidic networks. The flow-by 500–500 fluidic network exhibits a scaling close to $Re_w^{0.33}$ at low Reynolds numbers, as expected for flat solid electrodes under laminar flow conditions [40]. However, as the Reynolds number increases, the scaling starts to diverge from the laminar diffusion-limited scaling. This behaviour may be due to the increased pressure needed to flow the electrolyte at higher flow rates, allowing a bigger portion of fluid to enter the porous electrode [41]. The other three fluidic networks tested show a much steeper scaling, of roughly $Re_w^{0.74}$, through all the Reynolds numbers in the range studied. This difference in scaling regimes is an important indication of a significant change in the mechanism of mass transport within the porous electrode. We attribute the scaling improvement to the change between diffusion- to advection-dominated (observed numerically) when comparing to the benchmark flow-by design at the lower Reynolds numbers.

4.3. Electrochemical characterization at high concentrations

The efficacy of the mass transport enhancement of the proposed corrugated wall fluidic networks is further tested with concentrated electrolyte solutions (0.4 M $K_4Fe(CN)_6$ and 0.2 M 2,6-DHAQ) and the corresponding polarization curves are presented for volume flow rates of 100 ml min^{-1} and 300 ml min^{-1} in Fig. 5a and b. In order to eliminate the influence of fluctuations in the ohmic resistance of the cell between measurements and to directly compare the mass transport regions of the polarization curves, the polarization curves are presented in their IR-corrected forms (the raw polarization curves are given in Supplementary Figs. SI3a-d). In other words, to each voltage, the product of the ohmic resistance

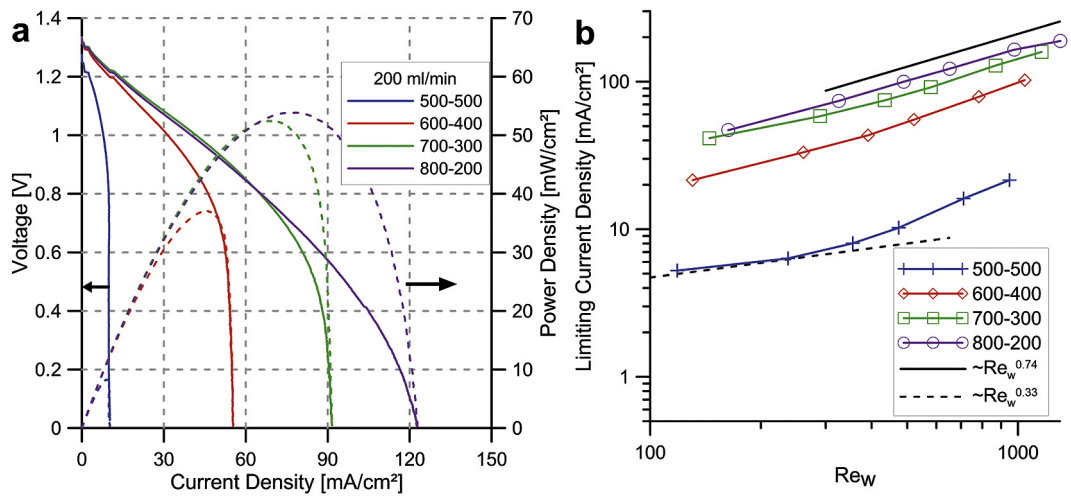

Fig. 4. Experimental polarization and power curves and limiting current scaling employing low concentration solutions (5 mM $K_4Fe(CN)_6$ and 2.5 mM 2,6-DHAQ). (a) Polarization and power curves of all tested designs at a volumetric flow rate of 200 ml/min. Polarization curves and power curves are shown in solid and dashed lines, respectively. (b) Scaling of the limiting current density with the Reynolds number. The Reynolds number Re_w is based on the hydraulic diameter of the narrowest section of the channel. The dotted line represents the scaling $Re_w^{0.33}$, while the solid black line represents the scaling $Re_w^{0.74}$. Symbols are included on the curves for every measured point.

Table 3
Comparison between theoretical and experimental limiting currents for dilute concentration conditions at a volumetric flow rate of 200 ml min^{-1} (5 mM $K_4Fe(CN)_6$ and 2.5 mM 2,6-DHAQ).

Theoretical limiting current (mA/cm^2)	Experimental limiting current (mA/cm^2)	Relative error
8.0	10.2	22%
21.8	55.3	61%
35.3	91.6	61%
55.2	122.4	55%

(measured via electrochemical impedance spectroscopy at 200 kHz) and the measured current is added the same way it was done in Ref. [15]. After this correction, the only two contributors to the deviation from a flat, ideal polarization curve are expected to be reaction kinetics and mass transport. Since the chemistry and the electrode employed do not change between the different experiments, the only attribute that makes a difference in the polarization curves presented is assumed to be mass transport.

From Fig. 5a and b we observe that there is a significant improvement in the mass transport characteristics when moving from the 500–500 (straight channels in flow-by configuration) design to the 800–200 (refer to the *d-w* labelling from Table 1 and Fig. 1b). The change between the 500–500 and the 600–400 polarization curves is rather abrupt for the mild difference between the two designs as previously noted in the low concentration results. This observation suggests, again, a change in the mechanism of mass transport from being heavily diffusion-limited to include advection as a more relevant factor. The evolution is less pronounced for higher flow rates as the polarization curves for all the different corrugated wall fluidic networks tend to collapse. Such a saturation behaviour indicates the exhaustion of the working principle and the start of a dominance of the reaction kinetics in the IR corrected polarization curves. Additionally, the evolution of the mass transport improvement starts to fade when moving towards narrower nozzles. The 500–500 case never reaches a very good performance even at flow rates as high as 300 ml min^{-1}. We attribute this fact to poor utilization of the porous electrode volume and localization of the reactions mostly near the interface between the free flow of electrolytes and the carbon paper. The power

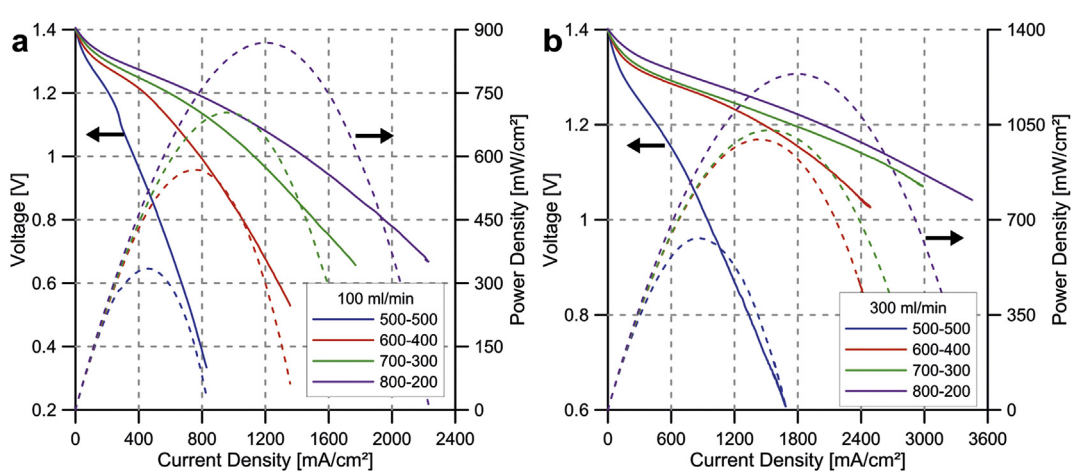

Fig. 5. Experimental IR-corrected polarization and non-IR corrected power curves for the four different designs employing high concentration solutions (0.4 M $K_4Fe(CN)_6$ and 0.2 M 2,6-DHAQ). (a) Volume flow rate of 100 ml/min. (b) Volume flow rate of 300 ml/min.

density produced also grows significantly with the use of the corrugated fluidic networks. The comparison between the 600–400 and the flow-by case shows an enhancement of 57% in maximum power produced. This enhancement can be of up to 96% when a comparison between the 800–200 design and the benchmark case is made. The results qualify the proposed fluidic networks as a viable option for power density enhancement in RFBs.

Comparing the maximum power taken from the IR-corrected polarization curves and the non-IR corrected power density curves for the 800–200 case at 300 ml min^{-1} (Fig. 5b), we notice the importance of ohmic resistance reduction to the overall performance improvement of redox flow cells. While the raw non-IR corrected power density curve shows a maximum value of roughly 1.2 W cm^{-2}, an ideal cell without ohmic resistance would result in a power density of 3.6 W cm^{-2} based on the results of Fig. 5b. Among the strategies to achieve smaller ohmic resistances, a reduction of the membrane resistance would be considered particularly beneficial for the electrochemical system studied in the present work. The membrane is likely to account for the biggest fraction of the ohmic resistance [27] due to the fact that it is not optimized for alkaline systems [42,43]. The Nafion 211 is one of the thinnest membranes available (nominal thickness of 25 μm) and decreasing the thickness further might compromise the separation of chemicals and affect the open-circuit voltage of the cell and mechanical stability of the membrane. Therefore, decreasing the membrane thickness would not be a viable option. Alternatively, a change in the flow battery chemistry to an acid-based electrolyte, like the all-vanadium redox system, would overcome this problem. However, a comparison between the two redox flow batteries chemistries with cell sizes comparable to the one presented here has yet to be realized.

4.4. Scaling of current density at high concentrations

Taking the experimental IR-corrected polarization curves for all flow rates (Fig. 5a and b and SI3a-d) into account, the current density at a potential of 1.2 V is plotted in Fig. 6 against the Reynolds number, defined in the same manner as for Fig. 4b.

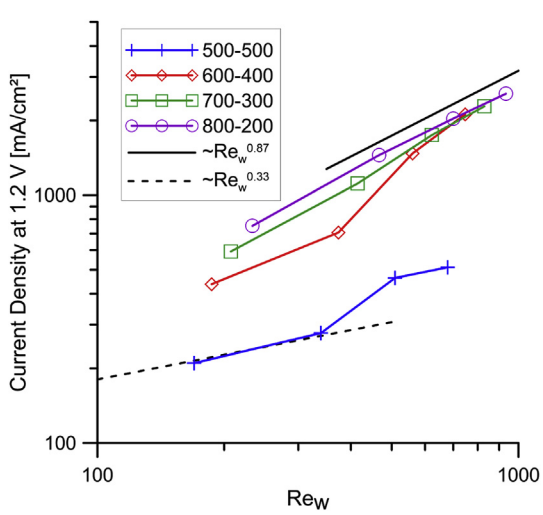

Fig. 6. Experimental dependency of the current density with Reynolds number for high concentration solutions (0.4 M $K_4Fe(CN)_6$ and 0.2 M 2,6-DHAQ) at an IR-corrected voltage of 1.2 V. The Reynolds number used is based on the hydraulic diameter of the narrowest section of the channel, Re_W. The dotted line represents a scaling of the current density with $Re_W^{0.33}$, while the solid black line represents a scaling of the current density with $Re_W^{0.87}$. Symbols are included on the curves for every measured point.

It is expected that the mass transport contribution vanishes as the Reynolds number tends towards infinity and the scaling of the current density with Reynolds becomes more closely determined by the stoichiometric limit (~Re^1). At the other extreme, when the Reynolds number tends to very small values, the mass-transport-related polarization is expected to become the main factor limiting the current density. With that in mind and observing the behaviour of the current density presented in Fig. 6, we notice a tendency towards a $Re_W^{0.87}$ scaling for high Reynolds numbers. This scaling is already very close to being linear, as expected for the stoichiometric limit. The points at the very bottom of the graph show a tendency, in the case of the parallel flow-by fluidic network, to follow the scaling $Re_W^{0.33}$. This scaling is an indication that the current density is under a laminar diffusion-dominated regime [40]. The rate at which the scaling of current density tends to the stoichiometric-limited regime is different for each design. For all the situations tested, the 800–200 design (refer to the nomenclature of Table 1 and Fig. 1b) follows the $Re_W^{0.87}$ scaling, from which we conclude that the transition to that behaviour occurs even below a Reynolds number of around 200. The 700–300 case has similar features, even though its transition to an almost linear scaling occurs at a higher Reynolds number. The small difference between the curves for the 700–300 and the 800–200 fluidic networks indicates a saturation of the benefit of mass transport enhancement as was observed previously with the IR-corrected polarization curves. For design purposes, this result is very important, since it leads to the conclusion that a further narrowing of the nozzles might be pointless from the point-of-view of an enhancement of mass transfer. As for the 600–400 design, the same type of transition as in the 700–300 case occurs at even higher Reynolds numbers and a regime with a smaller slope related to a mass-transport-dominated scaling is identified for small Reynolds numbers. The points with the smallest current densities are representative of the flow-by geometry with straight channels (here labelled 500–500). These points show a trend very close to a scaling with 1/3 in the two first measured points, while starting to transition to a regime more dominated by kinetics in further points. However, due to limitations of the experimental setup, no measurement at higher Reynolds numbers was done in order to identify a second scaling regime.

4.5. Net power density

With the effort of miniaturization, the pumping power and, consequently, the pressure drop gain importance when analysing the overall performance of redox flow cells. With that in mind, the pressure drop is measured for the four different designs using water as the working fluid (see Supplementary Fig. SI4). The pumping power is then theoretically calculated from this measurement by multiplying the flow rate by the measured pressure drop. Assuming laminarity of the flow, a correction is applied to account for the real viscosities of the electrolytes [18,27]. To allow a direct comparison with the produced power density, the result is normalized to the footprint of 1 cm^2.

To verify how the different designs deal with the balance between produced power and pumping power, the net power density is used as a figure of merit. It consists of the difference between the maximum produced power for a prescribed volumetric flow rate and the pumping power density associated with it ($P_{net} = P_{max} - P_{pump}$). The first could be readily obtained from the polarization curves (see Supplementary Figs. SI3a-d). However, slight variations in the ohmic resistance between the different assemblies could compromise the comparison of the fluidic networks from the perspective of mass transport only. Therefore, the polarization curves are IR-corrected using the mean measured value for

the ohmic resistance that is 0.344 Ω cm^2 across all cells. Fig. 7 shows the result, whereby the net power density at 400 ml min^{-1} for both the 700–300 and 800–200 designs are omitted because they are negative. In other words, these two situations require more pumping power than they are able produce with the electrochemical reactions.

Observing Fig. 7 in more detail, the flow-by configuration with straight channels configuration, even though generating the smallest pressure drop of all tested configurations, provides a smaller net power compared to the proposed corrugated wall configuration. The net power density curves for the corrugated designs show a clear range of volume flow rates for optimum application and also a shift of this optimum range towards smaller flow rates as the nozzle portion of the channel becomes narrower. This adjustable shift is the main advantage of the proposed fluidic networks in comparison with previously developed fluidic networks, like the interdigitated and the interdigitated with tapering. The mechanism for performance improvement is based on a continuous ratio between the widths of the widest and narrowest cross sections of the channel. This finding contrasts discrete alternatives with number of passes for the interdigitated design [19,26,27], for example. The novel corrugated channel design also allows for variation of the number of nozzles, adding to the parameters that can be used to further optimize the fluidic network. The effects of the number of nozzles has yet to be investigated, but it is expected to have a similar effect as multiple-passing for the interdigitated fluidic networks [27]. These two parameters open the opportunity to fine tune the fluidic network to accomplish optimum performance at an arbitrary operational volume flow rate, having the net power density as the main metric of performance.

Another interesting message from Fig. 7 is that the narrowing of the nozzle brings a net benefit when it comes to the maximum net power density regardless of the volume flow rate at which it occurs. Narrower channels are able to yield an ohmic-limited regime at lower flow rates (see Supplementary Figs. SI3a-d) and at the expense of similar pressure drops to broader ones at higher flow rates (see Supplementary Fig. SI4). But since the pumping power is the product of the pressure drop and the flow rate, the pumping power required to flow the electrolyte solutions will be considerably smaller. This finding is a good indicator that working at the lowest possible flow rate and tailoring a fluidic network for this purpose might be beneficial from the point-of-view of maximizing net power. However, this beneficial behaviour seems to fade as the difference in the maximum net power density decreases as one advances from the 500–500 design towards the 800–200 design. We attribute this finding to the facts that the produced power density also saturates as the cell becomes limited by ohmic resistance and the pumping power starts to become negligible at lower flow rates. The maximum net power density of the tested situations is attained with the 800–200 design and its value is 757 mW cm^{-2}, which represents a gain of 102% in comparison with the benchmark flow-by case.

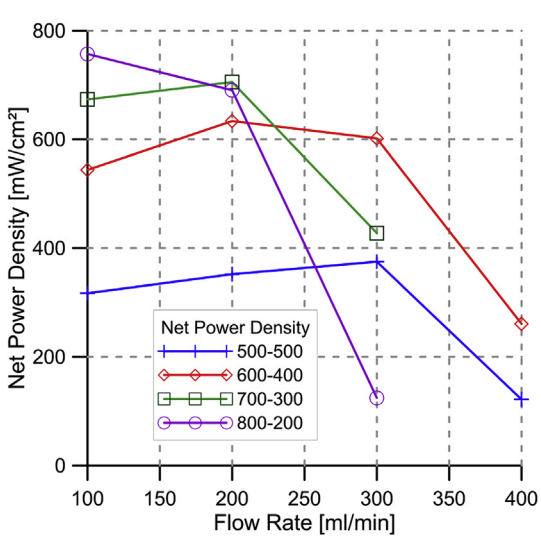

Fig. 7. Semi-empirical net power density variation with the volume flow rate. Behaviour of the maximum produced power density after subtraction of pumping losses ($P_{net} = P_{max} - P_{pump}$) for the four different fluidic networks as a function of flow rate. Symbols are included on the curves for every measured point.

5. Conclusions

We reported a facile and useful alternative to optimizing fluidic networks to specifically address the problem of mass transport polarization in miniaturized redox flow batteries.

A theoretical analysis showed and quantified the mass transport enhancement mechanism through regulating the constriction size of the channel corrugation. These fluidic networks caused a predicted 4× increase in limiting current density when comparing the 800–200 corrugated channel design to the flow-by parallel straight channel configuration.

The experiments with dilute concentrations proved a change in scaling of the limiting current with the Reynolds number from $Re_w^{0.33}$ (flow-by geometry at low Reynolds numbers) to $Re_w^{0.74}$, indicating a significant enrichment of the mass transport mechanism. The theoretical predictions were found to be inaccurate, predicting an increase of limiting current by 7× for the 800–200 corrugated fluidic network in comparison to the flow-by with straight parallel channels. This result considerably underestimates the experimentally determined enhancement of 12×. High concentration experiments were also conducted. The same abrupt improvement in performance based on the change from the flow-by design with straight channels to the 600–400 corrugated channel design was observed in IR-corrected polarization curves. Diminishing of the mass transport enhancement with progressive nozzle narrowing was present in all cases. With this we reach the conclusion that a further narrowing of the nozzles does not bring a significant benefit in produced power density to justify the added design complexity.

Investigating how the net power density varies with the volume flow rate, two main features were identified. The first is a shift in maximum net power density towards smaller volume flow rates with decreasing nozzle region size. Therefore, a fine adjustment of the maximum net power density is possible. The second is the increase of the maximum net power density with narrowing of the nozzles of the channels. These findings underscore the importance of this work, by enabling an optimized design to be realized for custom operational conditions when net power density is the key performance metric.

Acknowledgements

We gratefully acknowledge the Swiss National Science Foundation for financially supporting this work within the REPCOOL project (grant 147661). KML is grateful to the Brazilian funding agency CNPq for the financial support during his stay in Switzerland as an exchange PhD student (grant 207750/2015-7). We thank Lorenz Brenner for helping with the mounting of the setup and Jovo Vidic for the technical support.

Appendix A. Supplementary data

Supplementary data related to this article can be found at http://dx.doi.org/10.1016/j.jpowsour.2017.05.038.

References

[1] S. Chu, A. Majumdar, Opportunities and challenges for a sustainable energy future, Nature 488 (2012) 294–303, http://dx.doi.org/10.1038/nature11475.
[2] D. Larcher, J.-M. Tarascon, Towards greener and more sustainable batteries for electrical energy storage, Nat. Chem. 7 (2015) 19–29, http://dx.doi.org/10.1038/nchem.2085.
[3] W. Wang, Q. Luo, B. Li, X. Wei, L. Li, Z. Yang, Recent progress in redox flow battery research and development, Adv. Funct. Mater 23 (2013) 970–986, http://dx.doi.org/10.1002/adfm.201200694.
[4] J. Giner, L. Swette, K. Cahill, NASA TM-19760, National Aeronautics and Space Administration, U.S. Dept. of Energy, 1976.
[5] L.H. Thaller, NASA TM-79143, National Aeronautics and Space Administration, U.S. Dept. of Energy, 1979.
[6] M. Skyllas-Kazacos, F. Grossmith, Efficient vanadium redox flow cell, J. Electrochem. Soc. 134 (12) (1987) 2950–2953.
[7] A. Stephan, B. Battke, M.D. Beuse, J.H. Clausdeinken, T.S. Schmidt, Limiting the public cost of stationary battery deployment by combining applications, Nat. Energy 1 (2016) 16079, http://dx.doi.org/10.1038/nenergy.2016.79.
[8] C.S. Sharma, M.K. Tiwari, B. Michel, D. Poulikakos, Thermofluidics and energetics of a manifold microchannel heat sink for electronics with recovered hot water as working fluid, Int. J. Heat. Mass Transf. 58 (2013) 135–151, http://dx.doi.org/10.1016/j.ijheatmasstransfer.2012.11.012.
[9] P. Ruch, T. Brunschwiler, W. Escher, S. Paredes, B. Michel, Toward five-dimensional scaling: how density improves efficiency in future computers, IBM J. Res. Dev. 55 (2011), http://dx.doi.org/10.1147/JRD.2011.2165677, 15: 1–15:13.
[10] S. Govindan, D. Wang, A. Sivasubramaniam, B. Urgaonkar, Leveraging stored energy for handling power emergencies in aggressively provisioned datacenters, ACM SIGPLAN Not. 47 (2012) 75–86, http://dx.doi.org/10.1145/2248487.2150985.
[11] L.A. Barroso, J. Clidaras, U. Hölzle, The datacenter as a computer: an introduction to the design of warehouse-scale machines, second edition, Synth. Lect. Comput. Archit. 8 (2013) 1–154, http://dx.doi.org/10.2200/S00516ED2V01Y201306CAC024.
[12] W. Katsak, K. Le, T.D. Nguyen, R. Bianchini, Í. Goiri, Parasol and green switch: managing datacenters powered by renewable energy, SIGARCH Comput. Arch. News 41 (2013) 51–64, http://dx.doi.org/10.1145/2490301.2451123.
[13] T. Janoschka, N. Martin, U. Martin, C. Friebe, S. Morgenstern, H. Hiller, M.D. Hager, U.S. Schubert, An aqueous, polymer-based redox-flow battery using non-corrosive, safe, and low-cost materials, Nature 527 (2015) 78–81, http://dx.doi.org/10.1038/nature15746.
[14] M.L. Perry, A.Z. Weber, Advanced redox-flow batteries: a perspective, J. Electrochem. Soc. 163 (2016) A5064–A5067, http://dx.doi.org/10.1149/2.0101601jes.
[15] D.S.S. Aaron, Q. Liu, Z. Tang, G.M.M. Grim, A.B.B. Papandrew, A. Turhan, T.A.A. Zawodzinski, M.M.M. Mench, Dramatic performance gains in vanadium redox flow batteries through modified cell architecture, J. Power Sources 206 (2012) 450–453, http://dx.doi.org/10.1016/j.jpowsour.2011.12.026.
[16] Q.H. Liu, G.M. Grim, A.B. Papandrew, A. Turhan, T.A. Zawodzinski, M.M. Mench, High performance vanadium redox flow batteries with optimized electrode configuration and membrane selection, J. Electrochem. Soc. 159 (2012) A1246–A1252, http://dx.doi.org/10.1149/2.051208jes.
[17] B. Huskinson, M.P. Marshak, C. Suh, S. Er, M.R. Gerhardt, C.J. Galvin, X. Chen, A. Aspuru-Guzik, R.G. Gordon, M.J. Aziz, A metal-free organic-inorganic aqueous flow battery, Nature 505 (2014) 195–198, http://dx.doi.org/10.1038/nature12909.
[18] K. Lin, Q. Chen, M.R. Gerhardt, L. Tong, S.B. Kim, L. Eisenach, A.W. Valle, D. Hardee, R.G. Gordon, M.J. Aziz, M.P. Marshak, Alkaline quinone flow battery, Science 349 (80) (2015) 1529–1532, http://dx.doi.org/10.1126/science.aab3033.
[19] M.L. Perry, R.M. Darling, R. Zaffou, High power density redox flow battery cells, ECS Trans. 53 (2013) 7–16, http://dx.doi.org/10.1017/CBO9781107415324.004.
[20] Q. Chen, M.R. Gerhardt, L. Hartle, M.J. Aziz, A quinone-bromide flow battery with 1 W/cm^2 power density, J. Electrochem. Soc. 163 (2016) A5010–A5013, http://dx.doi.org/10.1149/2.0021601jes.
[21] R.A. Elgammal, Z. Tang, C.-N. Sun, J. Lawton, T.A. Zawodzinski, Species uptake and mass transport in membranes for vanadium redox flow batteries, Electrochim. Acta 237 (2017) 1–11, http://dx.doi.org/10.1016/j.electacta.2017.03.131.
[22] J.A. Trainham, J. Newman, A comparison between flow-through and flow-by porous electrodes for redox energy storage, Electrochim. Acta 26 (1981) 455–469, http://dx.doi.org/10.1016/0013-4686(81)87024-7.
[23] S. Kumar, S. Jayanti, Effect of flow field on the performance of an all-vanadium redox flow battery, J. Power Sources 307 (2016) 782–787, http://dx.doi.org/10.1016/j.jpowsour.2016.01.048.
[24] T. Jyothi Latha, S. Jayanti, Ex-situ experimental studies on serpentine flow field design for redox flow battery systems, J. Power Sources 248 (2014) 140–146, http://dx.doi.org/10.1016/j.jpowsour.2013.09.084.
[25] C.R. Dennison, E. Agar, B. Akuzum, E.C. Kumbur, Enhancing mass transport in redox flow batteries by tailoring flow field and electrode design, J. Electrochem. Soc. 163 (2015) A5163–A5169, http://dx.doi.org/10.1149/2.0231601jes.
[26] R.M. Darling, M.L. Perry, The Influence of electrode and channel configurations on flow battery performance, J. Electrochem. Soc. 161 (2014) A1381–A1387, http://dx.doi.org/10.1149/2.0941409jes.
[27] J. Marschewski, L. Brenner, N. Ebejer, P. Ruch, B. Michel, D. Poulikakos, 3D-printed fluidic networks for high-power-density heat-managing miniaturized redox flow batteries, Energy Environ. Sci. 10 (2017) 780–787, http://dx.doi.org/10.1039/C6EE03192G.
[28] G. McLean, N. Djilali, C.E.J. Reid, J. Lindstrom, W.R.M. Donis, Corrugated Flow Field Plate Assembly for a Fuel Cell, US 6544681 B2, 2003.
[29] J. Choe, K.H. Kim, D.G. Lee, Corrugated carbon/epoxy composite bipolar plate for vanadium redox flow batteries, Compos. Struct. 119 (2015) 534–542, http://dx.doi.org/10.1016/j.compstruct.2014.09.022.
[30] J.R. Hudkins, D.G. Wheeler, B. Peña, C.P. Berlinguette, Rapid prototyping of electrolyzer flow field plates, Energy Environ. Sci. 9 (2016) 3417–3423, http://dx.doi.org/10.1039/C6EE01997H.
[31] J. Noack, N. Roznyatovskaya, T. Herr, P. Fischer, The chemistry of redox-flow batteries, Angew. Chem. - Int. Ed. 54 (2015) 9776–9809, http://dx.doi.org/10.1002/anie.201410823.
[32] F. Pan, Q. Wang, Redox species of redox flow batteries: a review, Molecules 20 (2015) 20499–20517, http://dx.doi.org/10.3390/molecules201119711.
[33] J.A. Ochoa-Tapia, S. Whitaker, Momentum transfer at the boundary between a porous medium and a homogeneous fluid—I. Theoretical development, Int. J. Heat. Mass Transf. 38 (1995) 2635–2646, http://dx.doi.org/10.1016/0017-9310(94)00346-W.
[34] J.A. Ochoa-Tapia, S. Whitaker, Momentum transfer at the boundary between a porous medium and a homogeneous fluid—II. Comparison with experiment, Int. J. Heat. Mass Transf. 38 (1995) 2647–2655, http://dx.doi.org/10.1016/0017-9310(94)00347-X.
[35] B. Goyeau, D. Lhuillier, D. Gobin, M.G. Velarde, Momentum transport at a fluid–porous interface, Int. J. Heat Mass Transf. 46 (2003) 4071–4081, http://dx.doi.org/10.1016/S0017-9310(03)00241-2.
[36] D. Poulikakos, M. Kazmierczak, Forced convection in a duct partially filled with a porous material, J. Heat. Transf. 109 (1987) 653–662, http://dx.doi.org/10.1115/1.3248138.
[37] D.A.G. Bruggeman, Berechnung verschiedener physikalischer Konstanten von heterogenen Substanzen. I. Dielektrizitätskonstanten und Leitfähigkeiten der Mischkörper aus isotropen Substanzen, Ann. Phys. 416 (1935) 636–664, http://dx.doi.org/10.1002/andp.19354160705.
[38] D. Krishnamurthy, E.O. Johansson, J.W. Lee, E. Kjeang, Computational modeling of microfluidic fuel cells with flow-through porous electrodes, J. Power Sources 196 (2011) 10019–10031, http://dx.doi.org/10.1016/j.jpowsour.2011.08.024.
[39] D. Schmal, J. Van Erkel, P.J. Van Duin, Mass transfer at carbon fibre electrodes, J. Appl. Electrochem 16 (1986) 422–430, http://dx.doi.org/10.1007/BF01008853.
[40] W.A. Braff, C.R. Buie, M.Z. Bazant, Boundary layer analysis of membraneless electrochemical cells, J. Electrochem. Soc. 160 (2013) A2056–A2063, http://dx.doi.org/10.1149/2.052311jes.
[41] X. Ke, J.I.D. Alexander, J.M. Prahl, R.F. Savinell, Flow distribution and maximum current density studies in redox flow batteries with a single passage of the serpentine flow channel, J. Power Sources 270 (2014) 646–657, http://dx.doi.org/10.1016/j.jpowsour.2014.07.155.
[42] R.S. Yeo, J. McBreen, G. Kissel, F. Kulesa, S. Srinivasan, Perfluorosulphonic acid (Nafion) membrane as a separator for an advanced alkaline water electrolyser, J. Appl. Electrochem 10 (1980) 741–747, http://dx.doi.org/10.1007/BF00611277.
[43] G. Scibona, C. Fabiani, B. Scuppa, Electrochemical behaviour of nafion type membrane, J. Memb. Sci. 16 (1983) 37–50, http://dx.doi.org/10.1016/S0376-7388(00)81298-3.